Chapter 6
Design Considerations of Small-Animal CT Systems

Erik L. Ritman

1 Introduction

This chapter focuses on the ability of small-animal CT to provide information about molecular species and their spatial distribution in tissues. Over the past several decades radionuclide imaging methods have been the mainstay of in vivo molecular imaging by virtue of the variety of biologically active molecules that can be labeled with a radioactive marker. CT image data has been used to provide both attenuation correction of the SPECT and PET images as well as provide the anatomic localization of the radionuclide accumulation. This important contribution of CT to molecular imaging is presented in those chapters directly addressing the radionuclide imaging approaches. Although, the presence of higher atomic weight atomic labels (e.g., iodine) of biologically active tracer molecules can be conveyed by conventional X-ray attenuation-based imaging methods (in milli-molar concentrations as compared to pico-molar concentrations by radionuclide methods), molecular species can be conveyed by non-attenuating aspects of X-ray interaction with matter by virtue of their molecular bonds that are characteristic of polymeric molecules. These non-attenuating X-ray imaging methods are now starting to emerge from the feasibility demonstrations and hence will be explored in some depth in this chapter.

Micro-CT was first developed in the early 1980s [1–3]. In the later 1980s bench-top micro-CT was greatly facilitated by the development of a cone beam reconstruction algorithm by Feldkamp et al. [4] because the bench-top systems use the X-ray cone-beam to magnify the X-ray image itself.

Figure 6.1 is a schematic of a typical small animal CT scanner. CT is a 3D X-ray imaging method that involves obtaining X-ray projection images at many angles of view around an axis through an object and then applying a tomographic reconstruction

E.L. Ritman (✉)
Department of Physiology and Biomedical Engineering, Mayo Clinic College of Medicine, Rochester, MN, USA
e-mail: elran@mayo.edu

H. Zaidi (ed.), *Molecular Imaging of Small Animals: Instrumentation and Applications*,
DOI 10.1007/978-1-4939-0894-3_6,

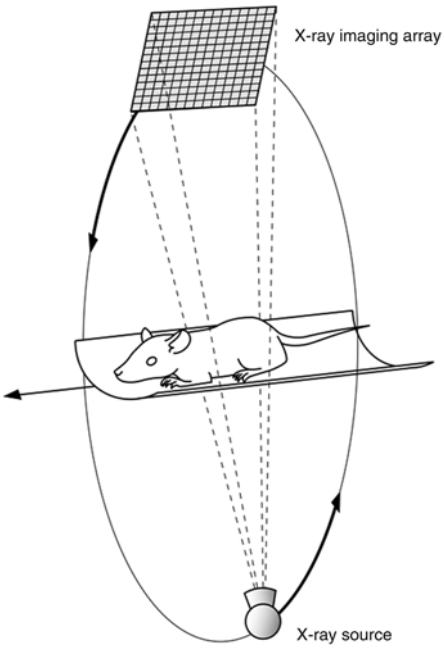

Fig. 6.1 Schematic of a small-animal CT scanner system. The small animal is anesthetized and lies on an horizontal table. If the animal's ECG and/or thoracic movement is monitored, then either prospective or retrospective gated scans and/or reconstructions can be performed by incremental recording/selection of the different angles of view required to generate transaxial CT images. The X-ray source and its opposite X-ray imaging array rotate about the cephalocaudal axis of the animal. Some scanners have dual X-ray source/detector arrays arranged at right angles to each other, which halves the scan time required. The animal table can be translated axially (i.e., at right angles to the plane described by the X-ray source trajectory) so that the length of the body scanned can be several times the length of animal exposed by the X-ray source [5]

algorithm to generate a stack of thin tomographic images of transaxial slices through the object. The transaxial images are made up of voxels (three-dimensional pixels).

Utilization and availability of small-animal CT systems has increased markedly over the past decade. It has evolved from custom-made scanners (applied mostly to imaging small-animal bones and segments of larger animal bones) to commercially available scanners designed for in vivo imaging of skeletal and soft tissues. Numerous reviews of the development and applications of micro-CT have been published [6–9]. A number of commercially marketed micro-CT scanners are now available for in-vivo small animal imaging. Some performance characteristics of a selected set of available small-animal CT scanners are summarized in Table 6.1. As this is a rapidly evolving market, this table is likely to be incomplete and in part obsolete in the not too distant future. Nonetheless, the message remains, in that the different functional characteristics of these scanners and the different imaging needs of the potential purchaser, will need to be carefully matched.

Table 6.1 Commercially-available small-animal CT scanners

Scanner	Diameter (mm)	Length (mm)	Voxel (μm)	kVp
Gamma Medica X-O	93	97	17	75
GE eXplore CT120	85	275	25–100	70–120
GE eXplore Lotus	55	275	27–90	70–120
Imtek micro-CATII	54	80	15–27	0–130
LaTheta LCT-200	30–120	300	24–60	80
ScanCo vivaCT 40	20–38	145	10–38	50–70
ScanCo vivaCT 75	40–78	145	20–79	50–70
SkyScan 1076 in vivo	68	210	9–35	20–100
SkyScan 1178	82	210	80–160	20–65

Similarly, because some scanners have a range of operational characteristics while others are more suitable for "turn-key" operation, an investigator will need to consider the positives and negatives of the operational flexibility of a scanner.

The grey-scale of those voxels is proportional to the attenuation coefficient of the material at the spatial location depicted by the voxel. The voxel is usually of the order of approximately 50–100 μm on-a-side when intact small animals are scanned—perhaps more appropriately called *mini-CT* because its CT images are scaled so as to provide voxel resolution such that the number of voxels per organ are similar to that obtained in human CT images. This generally involves clinical level X-ray photon energy. However, as small animals have higher heart and respiratory rates than humans do, scanning of the thorax involves scans that provide incremental scan data acquired over a number of sequential heart and/or respiratory cycles, so-called gated scanning. To provide CT image signal-to-noise comparable to clinical CT scanners the X-ray exposure of the animal or specimen should increase by an amount proportional to at least the inverse of the voxel volume [10–12]. As the radiation itself might affect the pathophysiology of interest in, for instance angiogenesis or cancer [6] a voxel size less than $(50\ \mu m)^3$ could result in excessive radiation exposure in living animals if repeated scans are involved.

True *micro-CT*, which has voxel resolution of the order of approximately 5–50 μm, is suitable for scanning isolated organs from small animals or tissue biopsies from larger animals or indeed intact dead small animals. For isolated specimens, for which higher resolution is often desired, the scanner generally operates at lower X-ray photon energy which is optimally matched to the diameter of the specimen [13].

In recent years several bench-top *nano-CT* scanners with sub-micrometer voxel resolutions have been developed and are commercially available. These can provide 3D images at cellular level of resolution, but scan only small volumes.

2 Rationale for Use of Small-Animal CT

CT has been used primarily to provide 3D images of anatomic structures and function of those structures by virtue of motion of those structures and/or of dynamic distribution of contrast agent within the vascular tree. Traditional clinical CT and

small-animal CT approaches have rarely been used to generate images of the spatial distribution of specific molecules by virtue of the CT image data itself. The uses of small-animal CT in biology include the following.

2.1 *Phenotype Characterization by Anatomic Structures and Material Composition*

Organ dimensions (e.g., dimensions of airways or volumes of lung, heart wall or chambers [14, 15]), bone mineralization [16, 17], micro-architecture of the cancellous bone and cortical bone thickness [18], blood vessel lumen diameter and branching geometry [19–21], tumor size and impact on its surrounding tissues (e.g., bone erosion or compression of adjacent blood vessels). Such measurements would be seen to change in response to maturation and/or disease or due to exposure to various pharmacological agents, environmental conditions or radiation exposure. These dimensions and local CT grey-scales can be measured directly from the 3D CT image data and thereby represent the main application of small-animal CT imaging to date.

2.2 *Physiological Spaces and Their Contents*

In addition to anatomic structures, especially entire organs, there are "macroscopic" physiological spaces such as the intravascular lumens, the lumens of ducts (e.g., renal tubules, ureters, bowel, bladder and bile ducts which tend to vary with time or pathophysiological conditions) or less well-defined microscopic spaces such as the extravascular space between the vessel endothelium and the parenchymal cells. This space swells with edema or with deposition of pathological proteins such as occurs in amyloidosis, or lipids such as occurs in atherosclerosis. These spaces can be detected and thereby delineated by use of contract agents which selectively accumulate (or avoid) those spaces. For the vascular tree iodinated-molecule solutions are used and bile and renal ducts can be opacified by virtue of intravascular injection of contrast agents that are selectively taken up and excreted by the liver or kidney respectively. Very transient labelling of those spaces can still be scanned despite the relatively slow micro-CT scans if incremental scans acquired from repeated contrast injections [22], use of long-duration contrast agent concentration in the blood stream [9] or snap-freezing of the tissue of interest for subsequent cryo-static scanning [23], are used to acquire the needed scan data. The volume of these spaces can be computed from the increase in CT values of those spaces.

2.3 Tissue Perfusion, Drainage and Secretion: Molecular Transport

Tissue perfusion (F) can be estimated from CT scans if they provide images at each heart cycle during the passage of a bolus of intravascular contrast agent [24]. Given the values of F and the extraction (e) of the contrast from the blood stream into the extra-vascular space, then the rate of influx or washout of the contrast agent from a physiological space can be used to estimate the transport into or out of that space from the Crone–Renkin relationship [25]: $PS = -F \cdot \ln(1 - e)$, where P is the endothelial permeability and S is the surface area of the endothelial surface. The value of S can be estimated from the intravascular blood volume of the microcirculation.

2.4 Need to Scan Entire Organ and Resolution

The volume that needs to be scanned is determined by several, sometimes conflicting, needs. Thus, we would need to scan an entire organ if we are looking for a focal lesion such as early cancer. On the other hand, at high voxel resolution it may technically not be possible to scan an entire organ at that resolution due to, for instance, limits on the X-ray detection system resolution and size. For estimation of organ volume, relatively large voxel sizes can be tolerated (e.g., a $(2\ \text{cm})^3$ heart needs approximately 4,000 voxels of $(30\ \mu\text{m})^3$ if better than a 1 % uncertainty is desired). However, if a 200 μm diameter basic functional units (i.e., BFU, the smallest accumulation of diverse cells that behave like the organ it is in, e.g., an hepatic lobule or a Haversian canal-centered osteome) is of interest, then voxel resolutions of better than $(100\ \mu\text{m})^3$ will be needed just to unambiguously detect it, but a $(3\ \mu\text{m})^3$ voxel would be needed if the volume of the BFU is to me estimated within 10 %.

3 Types of Small-Animal CT Approaches

The above considerations apply to most current uses of small-animal CT. These applications can also provide some information about atomic content and therefore relate to molecular discrimination and quantitation at only an indirect level. There are, however, other aspects of X-ray/matter interaction that can be used to discriminate and quantitate atom concentration as well as some chemical bonds, i.e., a more direct aspect of molecular characteristics.

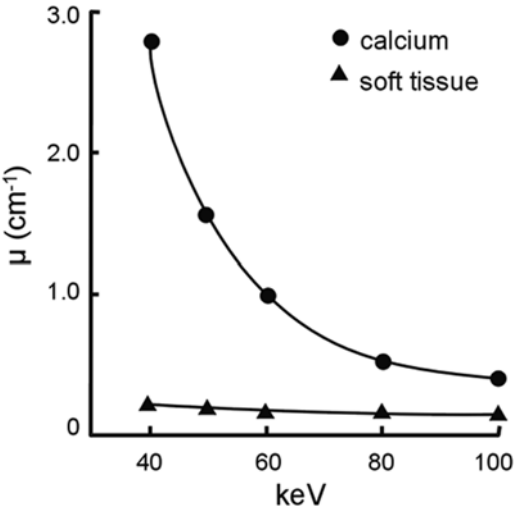

Fig. 6.2 Attenuation of X-rays passing through tissues differs depending on the tissue elemental content and the energy of the X-ray photons. In this example of a filtered 80 kVp source (effective 54 keV) the difference between calcium and soft tissue is dramatic. If the calcium is diluted so that its attenuation is comparable to the soft tissue, then by generating images at two energies, e.g., 80 and 50 keV, the Ca component will change more rapidly than the soft tissue, hence a subtraction of the two images will tend to leave a calcium signal but eliminate the tissue signal [26]

3.1 Attenuation-Based Scanning

This is the basis for the most common and most technically straightforward mode of CT scanning. The basic mechanism is the generation of a shadowgraph which is quantitated by measurement of the reduction in local X-ray intensity. By use of the Beer–Lambert law, $I = I_o \cdot e^{-\mu x}$, where I is the detected X-ray intensity at a detector pixel after passing through an object of thickness x, I_o is the incident X-ray intensity at the same pixel and μ is the attenuation coefficient of the specimen's material. As shown in Fig. 6.2 the attenuation coefficient (expressed as "/cm" of matter traversed) decreases exponentially with increasing X-ray photon energy up to an energy of up to approximately 50 keV due to the photo-electric effect (proportional to Z^3/E^3, where Z is the atomic number and E is the photon energy), beyond 50 keV μ decreases slowly with photon energy due to the Compton effect (largely independent of Z).

This image can be converted to a projection of the attenuation x thickness product (i.e., the line integral) along the X-ray beam traversing the object. With multi-angular projection data this can be mathematically converted to the three-dimensional distribution of the local attenuation coefficient at the site of each voxel making up the 3D image data set [27]. The X-ray beam should be monochromatic if beam hardening is to be avoided. This is readily achievable with a synchrotron [28, 29] by

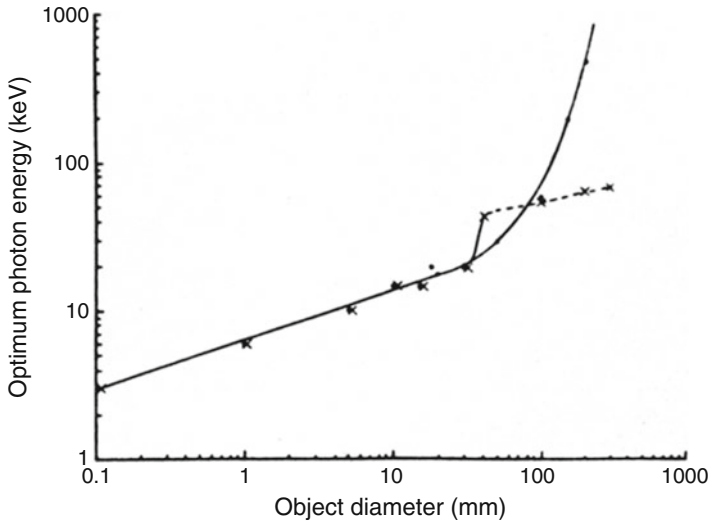

Fig. 6.3 The optimal photon energy for the detection of a 1 % density difference in circular water phantoms as a function of the diameter of the phantom. The diameter of the contrasting detail is 1/200 of the phantom diameter. Optimization criteria: *cross symbol*, minimum absorbed dose at center of phantom; *filled square*, minimum number of incident photons [31]

use of a diffraction crystal which can select those X-ray photons within a ±50 eV energy range. This can also be achieved in part by filtering the X-ray beam prior to it encountering the specimen. This generally involves use of a layer of aluminium which preferentially removes the lower energy photons, but if the K_α emission of the anode is to be used as the primary source (e.g., 17.5 keV for a Molybdenum anode), then a suitably matched filter with a Kedge absorption energy just greater than the K_α energy would also selectively reduce the photons with energy greater than the K_α energy [30] (e.g., 18 keV for a zirconium filter). This approach is effective but for the bench-top X-ray source results in a greatly diminished X-ray flux and hence requires long scan periods which are generally incompatible with in vivo scanning.

Finally, the signal (i.e., the change in local contrast of the shadowgraph) in all attenuation-based imaging approaches involves local reduction of X-ray intensity, which is accompanied by a reduced signal-to-noise ratio due to the reduction in the number of photons impinging on each detector pixel. Noise in this context is the variation of signal in adjacent pixels that should have identical signals due to the line integral of the specimen along the X-ray beam illuminating each pixel being identical. For specimens higher contrast resolution can be achieved by use of lower energy photons. As shown in Fig. 6.3, Spanne [31] showed that E has to increase with sample diameter (actually μx product) if noise is to be kept constant. Grodzins [13] showed that the optimal trade-off between signal and contrast resolution occurs when 10 % of the incident beam is transmitted. If the duration of the scan is important (especially in living animals) then higher X-ray photon energy is used because

of the higher signal (due to less attenuation). However, this is at the "cost" of lower "density" resolution.

This image can be converted to a projection of the attenuation x thickness product (i.e., the line integral) along the X-ray beam traversing the object. With multiangular projection data this can be mathematically converted to the three-dimensional distribution of the local attenuation coefficient at the site of each voxel making up the 3D image data set [27]. The X-ray beam should be monochromatic if beam hardening is to be avoided. This is readily achievable with a synchrotron [28, 29] by use of a diffraction crystal which can select those X-ray photons within a ±50 eV energy range. This can also be achieved in part by filtering the X-ray beam prior to it encountering the specimen. This generally involves use of a layer of aluminium which preferentially removes the lower energy photons, but if the K_α emission of the anode is to be used as the primary source (e.g., 17.5 keV for a Molybdenum anode), then a suitably matched filter with a Kedge absorption energy just greater than the K_α energy would also selectively reduce the photons with energy greater than the K_α energy [30] (e.g., 18 keV for a zirconium filter). This approach is effective but for the bench-top X-ray source results in a greatly diminished X-ray flux and hence requires long scan periods which are generally incompatible with in vivo scanning.

The absolute value and rate of decrease of attenuation coefficient differs depending on the element and the density of the material. Thus, the attenuation value of muscle tissue decreases 765-fold from 1 to 10 keV but only 31-fold from 10 to 100 keV whereas blood decreases 690 and 32-fold over the same ranges of photon energies. Subtracting the image obtained at a low from that obtained at higher photon energy would differentiate blood and muscle tissue better than their attenuation coefficient alone would at any one photon energy.

At 10 keV tissues of different density (e.g., fat, muscle and bone) show considerable differences in attenuation coefficients (3.1, 5.6 and 54/cm respectively) and hence can be distinguished from each other by their attenuation coefficient alone.

The attenuation coefficient can change dramatically at the so-called Kedge. As illustrated in Fig. 6.4 for iodine the attenuation coefficient increases from 6.55/cm to 35.8/cm when the photon energy increases by a mere electron volt at 33.1694 keV. Certain biologically relevant elements (such as iodine which occurs naturally in the thyroid gland or when purposely bound chemically to biological molecules of interest) can be identified and quantitated by subtracting images generated at a photon energy just below and just above the Kedge transition voltage. Unfortunately none of the common elements that occur naturally in the tissues of the body (e.g., Na, K, Ca, P etc.) have Kedges at sufficiently high keV photon energy that can be used for imaging of even isolated mouse organs, much less intact mice.

This is because at these very low photon energies (i.e., <10 keV) the attenuation of the X-ray is so large (i.e., only 0.5 % of photons pass through 1 cm of water—the thickness of a mouse abdomen) that useful images cannot be generated at acceptable radiation exposure levels.

This methodology generally involves use of either two energies of monochromatic photon radiation with narrow spectral bandwidth that "straddle" the Kedge

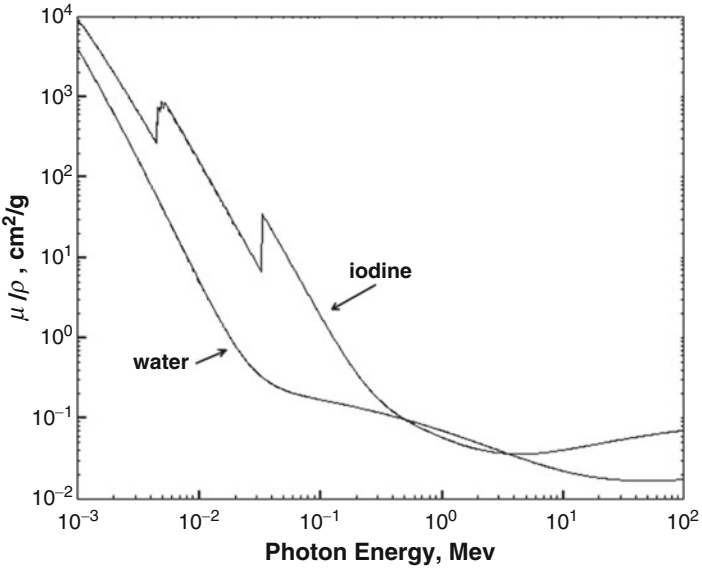

Fig. 6.4 Attenuation of X-ray, normalized for gravimetric density, by iodine decreases with increasing energy, but at approximately 5 and 33 keV there are step changes in attenuation. These are the so-called Ledge and Kedge of Iodine which correspond to the energy of the electrons in the L and K shells of the iodine atom. Water (the main component of living tissues) has those discontinuities due to the hydrogen and oxygen at 16 and 500 eV respectively, well below the X-ray photon energies used in small-animal-CT. Subtraction of two X-ray images involving X-ray photon energies at 32 and 34 keV would show a large difference in iodine signal but a relatively small change in the water signal—resulting in an essentially iodine-only image. Micromolar (15 μg/cm^3) concentrations of iodine can be detected by this method [32]

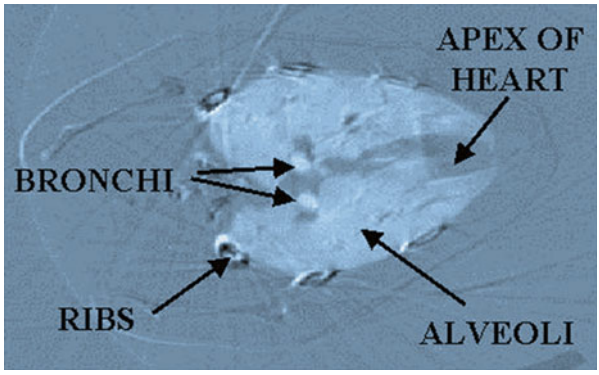

Fig. 6.5 A dual energy subtraction CT image of a rabbit lung obtained during inhalation of xenon gas (Kedge 34.56 keV). Note, the bright left and right bronchi and the less bright parenchymal signal of the xenon in the alveoli [33]

energy of the atom of interest or an energy selective X-ray detection system used with broad spectrum X-ray exposure. Narrowing of the spectral bandwidth (i.e., range of X-ray photon energy) down to levels of 50 eV can be achieved by use of a diffraction crystal at a synchrotron because even with this great restriction of X-ray flux there is still adequate X-ray flux to allow rapid imaging (Fig. 6.5).

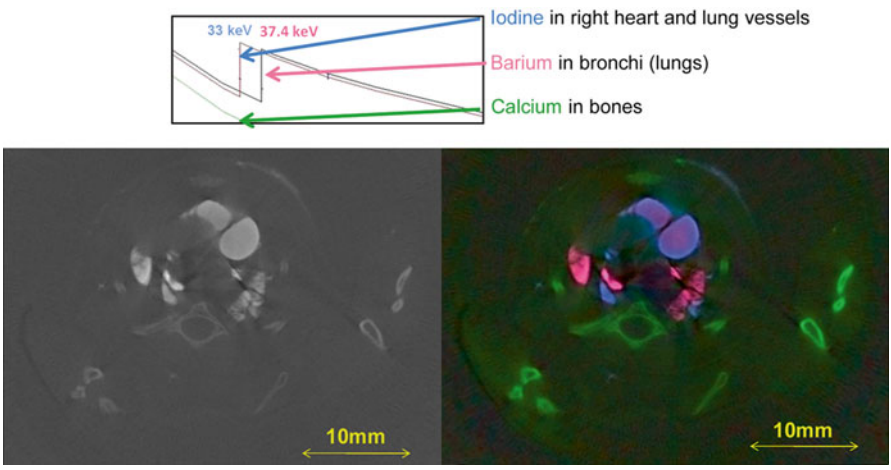

Fig. 6.6 *Left panel*: A CT image of a transaxial cross section of a mouse thorax. The bronchial tree had barium sulphate infused and the pulmonary artery had an iodine-based contrast injected. These different materials and the skeletal features cannot be distinguished unambiguously on the basis of their CT grey-scale values. *Right panel*: The use of Principal Component Analysis by virtue of the ability to extract the different X-ray photon energy components from the bremsstrahlung X-ray exposure allowed identification and quantitation of the three elements by virtue of their different attenuation-to-photon energy relationships—as illustrated in the *upper panel* [34, 35]

With conventional X-ray sources which produce broad spectrum bremsstrahlung suitable selection of the anode material for its characteristic K_α emission of the material, combined with a thin metal foil filter which has an absorption K edge just above the K_α photon energy, the spectral bandwidth can be reduced to 30 % or less. If an energy discriminating detector is used then those photons with energies of interest can be selected from the X-ray image data [34–38].

Recently detector arrays with 55 μm^2 pixels, energy discrimination and photon counting (up to 8,000 photons/s per pixel) have become available [34] for energies up to 18 keV (silicon-based array), 50 keV (GaAs array) and 75 keV (CdTe array) at 50 % detector efficiency (Fig. 6.6).

3.2 Fluorescence-Based Scanning

As shown in Fig. 6.7, elements that are irradiated with X-rays also fluoresce with X-ray photons that have an energy that is characteristic of that element. This so-called K_α emission also has low energy for most biological elements (e.g., Na 1 keV, P 2 keV, K 3.3 keV). However, by exposing a specimen to X-rays with photon energies higher than the K_α energy of the element of interest, chemically surrogate elements (e.g., Rb, a surrogate for potassium, has a K_α of 13.4 keV and Sr, a surrogate for Ca, has a K_α of 14 keV) or elements that can be used to label

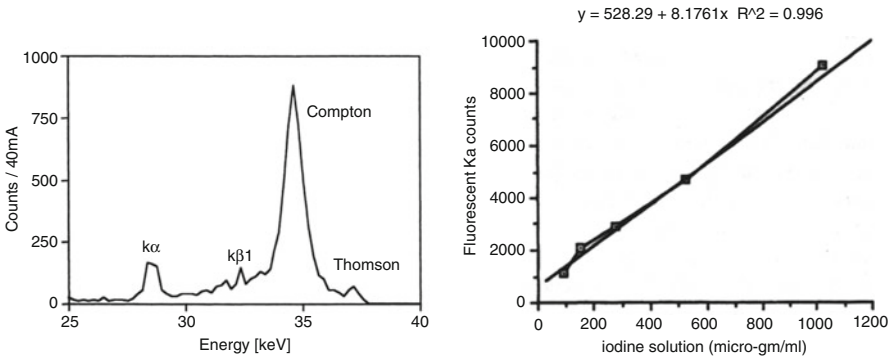

Fig. 6.7 *Left panel*: X-ray photon energy spectrum in scattered radiation measured at an angle to an illuminating X-ray pencil beam passing through an iodine solution. Thomson scatter is coherent and occurs at angles generally less than 15°. The energy is identical to the illuminating, 37 keV, X-ray beam. This deflection is used to generate a CT image of the location and concentration of a specific molecule. Compton scatter is predominant and its photon energy and intensity change with angle (0–180°) from the illuminating beam. The K_α and K_β peaks are the characteristic fluorescence of iodine. The intensity falls off with increasing angle to the illuminating X-ray beam. When the X-ray intensity at these peaks is used to generate a CT image, it is an image of the location and concentration of the element with that characteristic emission spectrum [39]. *Right panel* shows the linear relationship between the fluorescent counts and the concentration of iodine. Note that in attenuation-based CT the detectable concentrations are in the milli-molar range (10 mg/cm^3) rather than the micro-molar range (60 μg/cm^3) possible with fluorescence CT [40]

molecules or particles of interest (e.g., with Iodine which has a $K_\alpha = 28.5$ keV). This approach is particularly useful for detection of heavy metal contamination such as lead deposited in bone.

This approach can have several source/detector configurations, but as illustrated in Fig. 6.8, all detect the fluorescent X-rays at an angle to the illuminating beam. Thus, the regular transmission image can also be recorded during this scan.

If the fluorescence detector is sufficiently far from the object, then it will detect a line integral of emissions along each transilluminating pencil beam. If a collimated detector is used then each point along the transilluminated beam can have its emissions quantitated. This is straightforward if just a pencil beam is used because then the emissions are coming from a known location in the specimen. The only correction that has to be made is for the attenuation of the illuminating beam as it proceeds to the voxel of interest within the object and of the fluorescent emissions as they exit the specimen from that voxel. This can be done by use of the 3D attenuation map generated with the regular attenuation-based scan. To generate a 3D image would require scanning the X-ray beam transaxially relative to the object, which would require long scan durations. If, however, the specimen is illuminated with a thin, planar X-ray beam, along with a Suitable 2D collimator, then an axial plane of the specimen is illuminated, thereby speeding up the 3D scan process.

If the entire specimen is illuminated by, for instance, a cone beam of X-ray and observed with a multi-hole collimator, then each detector pixel records a line

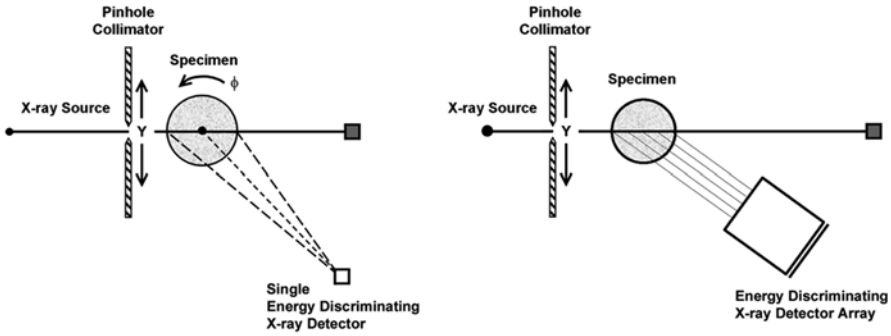

Fig. 6.8 Schematic of system for fluorescent X-ray tomographic imaging. *Left panel*: Involves trans-illuminating the specimen with a pencil beam of X-ray with narrow spectral bandwidth so that the lower photon energy K_α can be discriminated from the scattered X-ray. In order to generate the set of line-integral data needed for Radon-based tomographic reconstruction, this X-ray beam has to be translated across the specimen and this is repeated at each angle of rotation of the specimen about its axis. This is a very laborious process generally incompatible with live-animal scanning. *Right panel*: Involves a collimator which records the fluorescence from each location along the beam traversing the specimen so now no rotation of the specimen is needed to complete the scan of a single cross section. Indeed, a plane (oriented at right angles to the plane of the figure) is exposed then with a 2D collimator a volume can then be scanned in single rotation [41]

integral of fluorescence emissions, which would require multi-angular data, just as in a regular CT scan, to unravel the line integrals.

The fluorescent radiation is preferentially in the "forward" 2π steradians. This means that multiple detectors could be arranged around the transmission detector so as to decrease the duration of the scan because of the increased number of photons emitted at each point in the specimen being detected. Use of an energy discriminating detector system is needed to separate the Compton scatter from the fluorescent emissions.

3.3 Scatter-Based Scanning

Coherent scatter is a function of charge distribution within the scattering medium. As material with highly periodic charge distribution will scatter into well defined angles (so-called Bragg angles), various factors will tend to blur this discrete interference effect. Incoherent scatter can be separated from the coherent scatter by virtue of the fact that incoherent (i.e., Compton) scatter is diminished over the range of angles of importance for coherent scatter. Coherent scatter of X-rays which has the same photon energy as the illuminating X-ray and incoherent X-ray that has less energy than the illuminating beam. Figure 6.9 shows that these two scattering mechanisms distribute their photons over different solid angles relative to the illuminating beam.

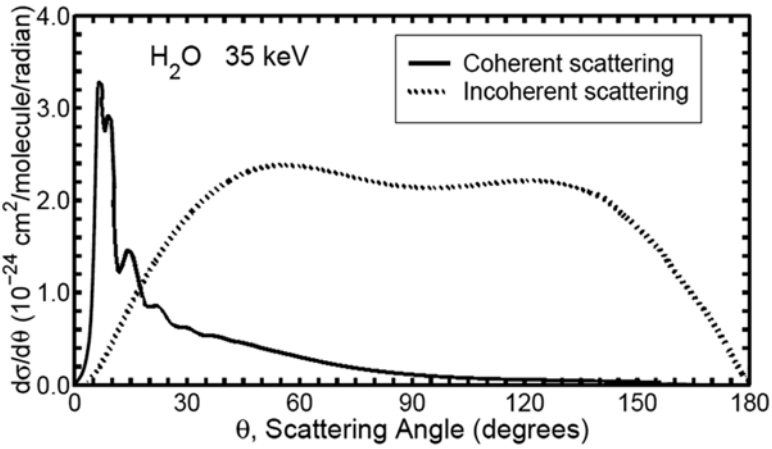

Fig. 6.9 Two mechanisms of X-ray scattering—coherent scatter has photon energy equal to that of the illuminating beam and is limited to approximately 0–15° from the illuminating beam, the actual angular distribution being dependant on the illuminating photon energy and the chemical bonds in the material. Incoherent (Compton) scatter has photon energy less than that of the illuminating beam. Its angular distribution is essentially constant over all but the acute and obtuse angles relative to the illuminating beam [42]

The scanner arrangement and subsequent processing of the detected signals is very similar to that of the fluorescence approach. The angular distribution of the coherent X-ray scatter is characteristic for different materials, especially for polymeric molecules such as collagen by virtue of the repetitive nature of the chemical bonds which have lengths of the order of an X-ray wavelength.

As illustrated in Fig. 6.10, the angle-dependant pattern of coherent X-ray scatter is characteristic for the material being illuminated. This pattern is called the momentum transfer curve (q).

It is generally generated by observing the scatter over a range of angles θ. Use of an energy-discriminating detector system can be used to reduce (or even eliminate) the need for multiple angles of view because $q=(1/\lambda)\sin(\theta/2)$ where λ is the X-ray photon wavelength and θ is the angle between the illuminating X-ray beam and the scatter direction can also be represented by $q=(E/12.3)\sin(\theta/2)$ where θ is fixed and the range in photon energy E (keV) is provided by the breakdown of the broad X-ray spectrum into a number of energy "bins". The energy discrimination could also help separate the Compton scatter from the coherent scatter.

This characteristic curve can be used to identify the material. Molecules with strings of repetitive chemical bonds include proteins (e.g., collagen) and synthetic materials such as often used in prosthetic devices made of synthetic polymer-based materials. The wavelength of the K_α X-ray emission of tungsten is 20 pm and of molybdenum is 71 pm, hence it is repetitive structures such as chemical bonds (e.g., C–C 154 pm, C–H 109 pm) that produce strong coherent scatter patterns. As shown in Fig. 6.11, collagen or protein, which contain strings of repetitive chemical bonds,

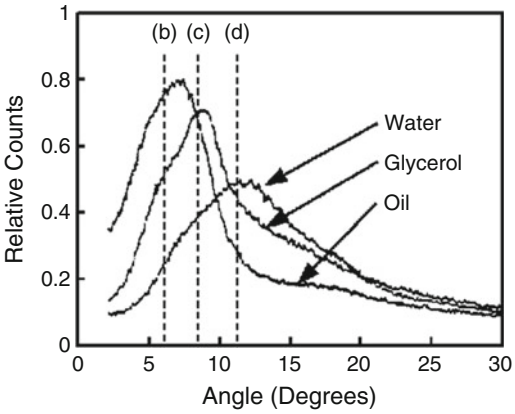

Fig. 6.10 X-ray scatter curves (more generally expressed as momentum transfer curves in which the X-ray wavelength is also accounted for) recorded from water, glycerol and oil which were illuminated by a pencil beam of 17.5 keV X-rays. Even though these curves were not corrected for the Compton scatter contribution, the different curves clearly allow discrimination of glycerol and oil which have very similar attenuation coefficients [43]

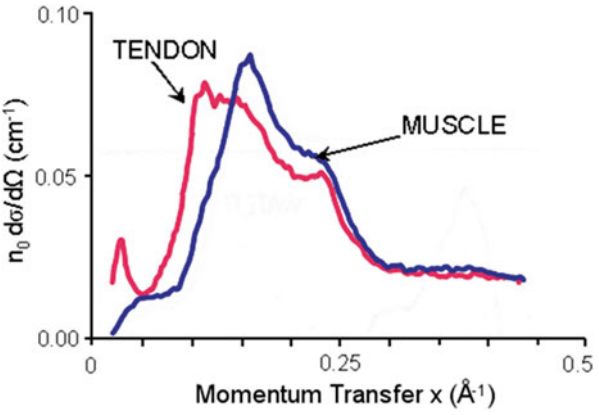

Fig. 6.11 Two momentum transfer curves—one from muscle and one from tendon. The greater collagen content of the tendon shifts the peak of the curve to the left (by a ratio of 0.47) and thus allows discrimination of muscle from tendon more readily than is possible by conventional coefficients of tendon and muscle [45]

differ distinctly in their scattering characteristics. Attenuation coefficients differ by a ratio of 0.02 of clinical kVp levels [44].

Different collagen types differ in their X-ray scattering characteristics such as occurs when the collagen is malformed in cancerous tissues, can be detected [46]. This is perhaps the most promising aspect of X-ray imaging with respect to the ability to detect and discriminate a variety of molecules directly with X-ray imaging. At this stage imaging of coherent X-ray scatter has been demonstrated only in test phantoms and isolated tissue specimens. Thus, the peak coherent scattering intensity for tendon was found to be approximately at a momentum transfer value of 10 Å^{-1} whereas skeletal muscle had a value of 17 Å^{-1} [45]. Unfortunately, due

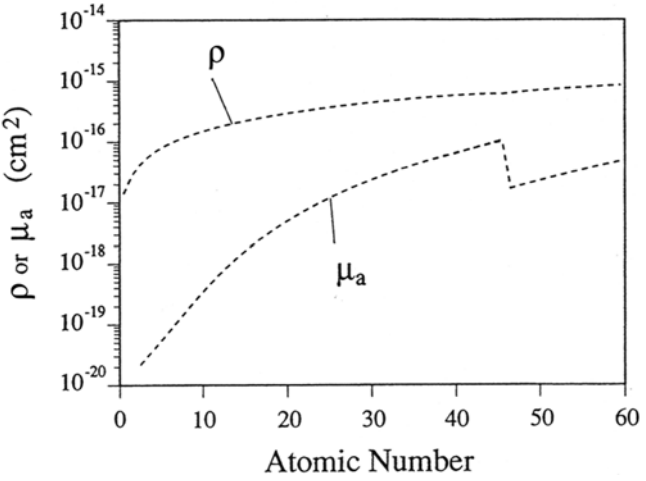

Fig. 6.12 Atomic X-ray phase shift (ρ) and absorption (μ) of 24 keV X-ray as a function of atomic number. The X-ray refractive index of matter $n = 1 - \delta - i \cdot \beta$, where δ is the phase shift related component and β the attenuation related component. The step-change in the absorption curve corresponds to the Kedge effect. Note that the ρ value is orders of magnitude higher than the μ value at any one atomic number, indicating that either the X-ray refractive properties of matter can either be exploited to provide higher contrast resolution or reduced radiation exposure [47]

to the low signal-to-noise of this imaging approach at the radiation levels tolerable in living animals, scatter-based CT is probably practical only when the accumulation of the molecules of interest are locally widespread (so that large voxels can be used to increase signal-to-noise) and concentrated. These conditions are most likely to be achieved with pathological accumulations of proteins such as in amyloid disease and when applied to imaging prosthetic device materials (especially when the μ of the prosthetic material is close to the μ of the surrounding tissues) in living small animals.

3.4 Phase Contrast Scanning

X-rays, like light, are refracted by matter, resulting in slight deviations of the X-ray beam from its initial straight-line trajectory. However, the refractive index of X-ray in water is very small, 7.4×10^{-7} [46]. Nonetheless, as shown in Fig. 6.12, the phase-shift component (δ) of the refractive index is orders of magnitude greater than the attenuation component (β) of the compound refractive index n: $n = 1 - \delta - i \cdot \beta$, where $i = \sqrt{-1}$. At 17.5 keV there is a 180° phase shift caused by 50 μm of tissue whereas the change in attenuation caused by 50 μm water is only 0.25 %.

The deflection of the X-ray results from a shift in the phase of the X-ray, which in turn is the result of the X-ray's interaction with the molecular structure of the

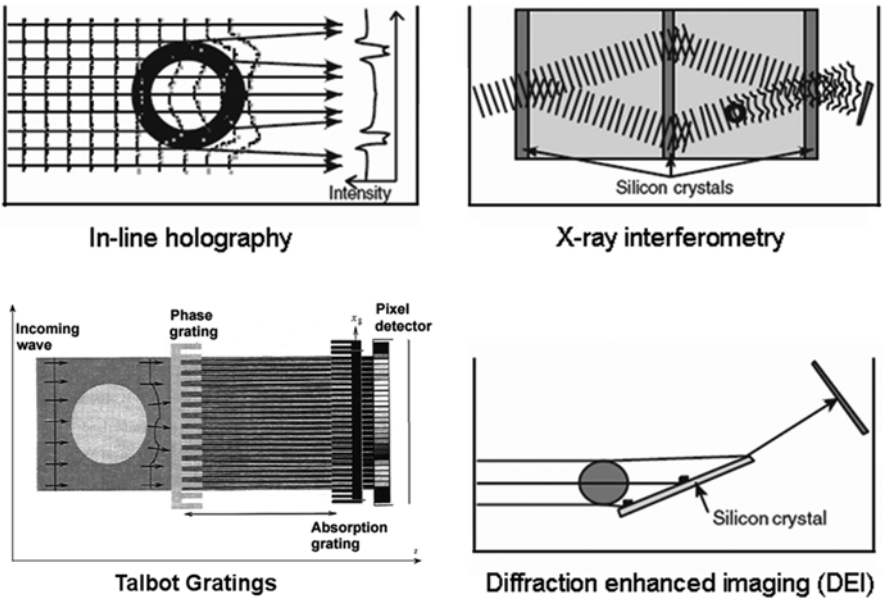

Fig. 6.13 Four methods of using the very slight deviation of X-ray due to change in refractive index of material along the path of an X-ray beam. This effect can also be detected quantitatively by virtue of the phase shift of the X-ray. *Left upper panel* shows how the slight deviation of the X-ray can be used by inverting the image data obtained in many views around the object [48]. This method involves placing the detector array at increasing distance away from the X-ray source. The change in local image brightness distribution can then be used to deduce the refraction at each location in the transmitted X-ray image. *Right upper panel* shows how use of the interference between the phase of a reference beam and the beam transmitted (and phase shifted) by an object can be used to generate a moiré pattern that can be "unravelled" to provide the local phase shift in the transmitted beam [49]. *Right lower panel* shows how a silicon crystal diffractometer can be used to directly measure the small angular deflection of individual X-ray beams by rocking the crystal [50]. *Left lower panel* shows how gratings can be used to generate "coded" X-ray images such that the distortion of that coded image by the phase shift can then be used to estimate the local refraction [51]

material. Phase shift cannot be measured directly with imaging systems because the frequency of approximately 10^{18}/s is much too fast. However, phase shift can be detected much more readily by virtue of interference patterns that can be generated by several means. This can be achieved by four methods as illustrated in Fig. 6.13 The first demonstration of this approach involved use of a parallel beam of narrow bandwidth monochromatic X-ray that is split into a reference beam which bypasses the specimen so that the interference pattern generated by mixing the reference beam and the beam passing through the specimen can be used to generate a map of the line integrals of phase shift at each angle of view.

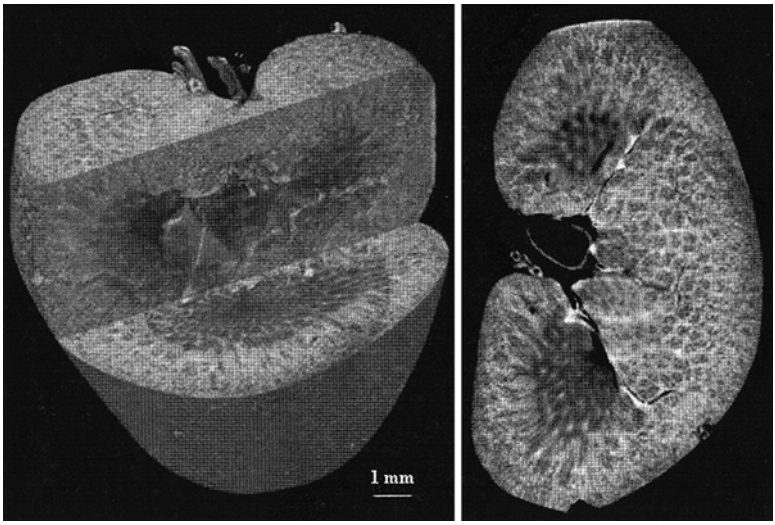

Fig. 6.14 Phase-contrast X-ray CT image of rat kidney obtained at 35 keV. Whole structures of renal cortex, medulla and pelvis were observed [59]

This method is very effective but would be technically very difficult to scale up for intact animals or large tissue specimens. Another method involves using a Bragg diffraction crystal which is used to differentiate the very slight angle between the refracted and transmitted X-ray beam. This also requires a parallel beam of very narrow bandwidth X-rays and involves rotating (rocking) the analyzer crystal over a range of angles to generate the multiple images of X-ray intensities at each angle of view about the specimen and for each pixel at that angle of view around the specimen.

The most practical method, and the method that most readily can accommodate a broad spectrum, non-parallel X-ray beam, involves use of multiple venetian blind-like gratings (for instance consisting of micrometer wide layers of gold on silicon) placed between the source and specimen (to convert the full area beam into a series of parallel linear sources) and between the specimen and the detector array (to analyze the transmitted X-ray image). The slight deflection of the X-rays due to the refraction in the specimen can be quantitatively detected by moving the analyzer grating across the image in steps that are fractions of the interval between adjacent slats in the source grid, much like the function of a vernier micrometer [52–58]. Figure 6.14 is an example of the high contrast that is achievable with this methodology [59].

The phase shift can be shown to be proportional to mass density for most biological materials, except when there is a high proportion of hydrogen present which has almost double the effect on phase due to its unique electron charge to Z ratio.

4 Technical Issues

If the X-ray source/detector system is stationary (which is always true if the X-ray source is a synchrotron) and the specimen is rotated, then this has the advantage that the heavy components of the scanner can be rigidly and accurately positioned with great precision. This works very well for in vitro specimens, but this generally involves use of a vertical rotation of the specimen (rather than horizontal) as this minimizes the gravity-induced movement or distortion of the specimen, relative to its axis of rotation. The living animal and its contents cannot be secured sufficiently rigidly to prevent motion as it rotates about a horizontal axis. While rotation of a living animal about a vertical axis minimizes this problem, maintenance of a vertical position over an extended period of time is not physiological for larger quadrupeds and may interfere with cardiopulmonary function, although it is generally acceptable for small rodents.

Rotation of the X-ray source/detector system about a horizontal axis ensures that the animal is in its physiological horizontal position, and thus it will not distort with angle of view. A technical requirement for this arrangement is that the generally heavy source/detector components have to rotate so that deviation from the ideal trajectory about the axis of rotation is smaller than the detector pixel size.

The duration of a complete scan depends on the X-ray flux that can be generated by the X-ray source as this governs the duration required to generate a projection image of sufficient quality (i.e., signal-to-noise and motion blurring) to be used for tomographic imaging and to a lesser extent the speed with which the necessary X-ray detection information can be recorded and transferred to an off-scanner memory. These factors vary greatly depending on the specific X-ray modality used to generate the tomographic image data.

If a synchrotron is used to generate the X-ray, then this very brilliant source can be used to generate a very narrow bandwidth monochromatic X-ray beam [60]. State-of-the-art synchrotrons can generate monochromatic X-ray beams of up to 100 keV photon energy. This beam can be sufficiently intense that the main factor in the duration of the scan is the time required for image recording and transfer to a memory. The method is also limited in the width and height of the field-of-view that is exposed by X-ray. If a bench-top roentgen X-ray source is used then the divergence of the X-ray beam can be used to expose a large field-of-view. However, use of a point-source X-ray the cone-beam geometry introduces some mathematical complications which may limit the resolution of the tomographic images at the upper and lower axial extents of the specimen. This effect is largely overcome by combining a translation with the rotation trajectory, most commonly achieved by either a “step and shoot”, in which the animal is advanced one axial field-of-view length after completing each sequential scan. The helical CT scanning mode, in which the specimen is translated along the axis of rotation during the scan, allows coverage over a long axial extent but this reduces the temporal resolution of the tomographic image data set.

5 Radiation Exposure

X-ray exposure results in direct disruption of chemical bonds and generates super radicals which in turn damage near by molecules, the DNA being of particular concern as this affects cell reproduction and its control [11, 61–63]. The number of photons absorbed in a voxel determines the noise in the CT image (i.e., the variation in grey scale from voxel-to-voxel differs even though they represent the same material). For a given exposure of the subject the number of photons interacting within a voxel decreases in direct relationship with the voxel volume. This, combined with some other consequences of the scanning process, results in the radiation exposure to the subject having to increase with the fourth power of the voxel side dimension if the noise per voxel is to remain unchanged [10]. Consequently, the higher the spatial resolution the higher the radiation exposure. The LD50/30 dose (following which 50 % animals die within 30 days) for small animals is somewhat less than eight Grey. A scan generating $(65\ \mu m)^3$ voxels would involve five Grey exposure [63], tolerable in a terminal study, but not in the first of several sequential scans of the same animal in a longitudinal study.

6 Conclusions

Molecular structure, in terms of elemental components (either as part of the molecule or as a synthetically labeled molecule) and certain chemical bonds (especially if they repeat along the length of long molecules) can be detected and somewhat characterized by X-ray micro-CT imaging methods. Conventional, attenuation-based, micro-CT often plays an integral part of non-attenuation-based micro-CT, because it provides the high spatial resolution confines of organs and physiological spaces in which molecules of interest tend to be confined, excluded or washout from and it provides the spatial distribution of X-ray attenuation that is needed to correct the non-attenuation-based micro-CT image data for attenuation of the X-ray used for image generation using the non-attenuation aspect.

Although the attenuation aspect and the other modalities can readily be individually integrated into a single micro-CT scanner, so that time is saved and more importantly that registration of the two different images is greatly facilitated, no one micro-CT combination is likely to meet all needs.

A major strength of small-animal-CT is that it provides clinically relevant image information of pathophysiology, both at scale-equivalent of clinical CT scan resolution. Micro-CT can provide image data at resolutions much higher than achievable with clinical scanners so that deeper insights into pathophysiological processes can be expected. Another strength of small-animal-CT is that it provides a test-bed for development and evaluation of novel, clinically applicable, X-ray imaging approaches.

Acknowledgments Dr. Ritman's micro-CT work was supported in part by National Institutes of Health Grant, EB000305.

References

1. Elliot JC, Dover SD (1982) X-ray tomography. J Microsc 162(2): 211–213.
2. Flannery BP, Deckman HW, Roberg WG et al (1987) Three dimensional x-ray microtomography. Science 237: 1439–1444.
3. Sasov A (1987) Non-destructive 3D imaging of the objects internal microstructure by microCT attachment for SEM. J Microsc 147: 169–192.
4. Feldkamp LA, Davis LC, Kress JW (1984) Practical cone-beam algorithm. J Opt Soc Am A1: 162–191.
5. Ritman EL (2014) Cone beam micro-CT for small-animal research. IN: Shaw C (ed): Cone Beam Computed Tomography. Chapter 12, pp171–179. CRC Press (Taylor and Francis).
6. Paulus MJ, Geason SS, Kennel SJ et al (2000) High resolution x-ray tomography: an emerging tool for small animal cancer research. Neoplasia 2: 36–45.
7. Holdsworth DW, Thornton MM (2002) Micro-CT in small animal and specimen imaging. Trends Biotech 20(8): S34–39.
8. Ritman EL (2004) Micro-computed tomography: Current status and developments. Annual Rev Biomed Eng 6: 185–208.
9. Badea CT, Drangova M, Holdsworth DW et al (2008) In vivo small-animal imaging using micro-CT and digital subtraction angiography. Physics in Med Biol 53: R319–R350.
10. Brooks RA, Di Chiro G (1976) Statistical limitations in x-ray reconstructive tomography. Med Phys 3: 237–240.
11. Ford NL, Thornton MM, Holdsworth DW (2003) Fundamental image quality limits for micro-computed tomography in small animals. Med Phys 30: 2869–2898.
12. Faulkner K, Moores BM (1984) Noise and contrast detection in computed tomography images. Phys Med Biol 29: 329–339.
13. Grodzins L (1983) Optimum energies for x-ray transmission tomography of small samples. Nucl Instrum Methods 206: 541–545.
14. Drangova M, Ford NL, Detombe SA et al (2007) Fast retrospectively gated quantitative four-dimensional (4D) cardiac microcomputed tomography imaging of free-breathing mice. Invest Radiol 42: 85–94.
15. Badea CT, Hedlund LW, Johnson GA et al (2004) Micro-CT with respiratory and cardiac gating. Med Phys 31: 3324–3329.
16. Cowan CM, Aghaloo T, Chou YF et al (2007) Micro-CT evaluation of three dimensional mineralization in response to BMP-2 doses in vitro and in critical sized rat calvarial defects. Tissue Eng 13: 501–512.
17. Borah B, Ritman EL, Dufresne TE et al (2005) The effect of residronate on bone mineralization as measured by micro-computed tomography with synchrotron radiation: Correlation to histomorphometric indices of turnover. Bone 37(1): 1–9.
18. Kinney JH, Lane NE, Haupt DL (1995) In vivo three dimensional microscopy of trabecular bone. J Bone Miner Res 10(2): 264–270.
19. Lee J, Beighley P, Ritman E et al (2007) Automatic segmentation of 3D micro-CT coronary vascular images. Med Image Analysis 11(6): 630–647.
20. Op den Buijs J, Bajzer Z, Ritman EL (2006) Branching morphology of the rat hepatic portal vein tree: A micro-CT study. Ann Biomed Eng 34(9): 1420–1428.
21. Nordsletten D, Blackett S, Bentley MD et al (2006) Structural morphology of renal vasculature. Am J Physiol: Heart Circ Physiol 291: H296–H309.
22. Badea CT, Hedlund LW, Mackel JF et al (2007b) Cardiac micro-computed tomography for morphological and functional phenotyping of muscle LIM protein null mice. Mol Imaging 6: 261–268.
23. Kantor B, Jorgensen SM, Lund PE et al (2002) Cryostatic micro-computed tomography imaging of arterial wall perfusion. Scanning 24: 186–190.
24. Schmermund A, Bell MR, Lerman LO et al (1997) Quantitative evaluation of regional myocardial perfusion using fast x-ray computed tomography. Herz 22(1): 29–39.

25. Crone C (1963) The permeability of capillaries in various organs as determined by the use of the indicator diffusion method. Acta Physiol Scand 58: 292–305.
26. Cann CE, Gamsu G, Birnbert FA et al (1982) Quantification of calcium in solitary pulmonary nodules using single and dual-energy CT. Radiology 145: 493–496.
27. Herman GT (1980) Image Reconstruction from Projections: The Fundamentals of Computerized Tomography. Academic Press, New York.
28. Dilmanian FA (1992) Computed tomography with monochromatic x-rays. Am J Physiol Imaging 7(3-4): 175–179.
29. Bonse U, Johnson Q, Nicols M et al (1986) High resolution tomography with chemical specificity. Nucl Instrum Methods Phys Res A 246(1-3): 644–648.
30. Ross PA (1928) A new method of spectroscopy for faint x-radiations. J Opt Soc Am 16: 433–437.
31. Spanne P (1989) X-ray energy optimization in the computed tomography. Phys Med Biol 34(6): 679–690.
32. http://physics.nist.gov/PhysRefData/XrayMassCoef/
33. Le Duc et al (1999) ESRF HighLights. http://www.esrf.eu/UsersAndScience?Publications/Highlights/1999/life-sci/broncho.html
34. Butzer JS, Butler APH, Butler PH et al (2008) Image and Vision Comput New Zealand, pgs. 1-6, doi:10.1109/IVNZ.2008.4762080.
35. Anderson NG, Butler AP, Scott N et al (2009) Medipix imaging – evaluation of data sets with PCA. Eur Radiol B-393: S228.
36. Panetta D, Belcari N, Baldazzi G et al (2007) Characterization of a high-resolution CT scanner prototype for small animals. Nuovo Cimento B 122: 739–747.
37. Firsching M, Butler AP, Scott N et al (2009) Contrast agent recognition in small animal CT using the Medipix2 detector. Nucl Inst Meth A 607: 179–182.
38. Gleason SS, Sari-Sarraf H, Paulus MJ et al (1999) Reconstruction of multi-energy x-ray computed tomography images of laboratory mice. IEEE Trans Nucl Sci 46: 1081–1086.
39. Takeda T, Yuasa T, Hoshino A et al (1997) Fluorescent x-ray computed tomography to visualize specific material distribution. IN: Developments in X-ray Tomography. Proc SPIE 3149: 160–172.
40. Takeda T, Tu Q, Yashiro T et al (1999) Human thyroid specimen imaging by fluorescent x-ray computed tomography with synchrotron radiation. Proc SPIE 3772: 258–267.
41. Cui CW, Jorgensen SM, Eaker DR et al (2008) Coherent x-ray scattering for discriminating biocompatible materials in tissue scaffolds. Proc SPIE: Development X-ray Tomogr VI 7078: 70781S-1-70781S-10.
42. Johns PC, Leclair RJ, Wismayer MP (2002) Medical x-ray imaging with scattered photons. IN: Opto-Canada: SPIE Regional Meeting on Optoelectronics, Photonics, and Imaging, Proc SPIE TDO1:355–357.
43. Grant JA, Morgan MJ, Davis JR et al (1993) X-ray diffraction microtomography. Meas Sci Technol 4: 83–87.
44. Pelc JS (2001) Volume rendering of tendon-bone relationships using unenhanced CT. Am J Roentgenol 176: 973–977.
45. Kosanetzky J, Knoerr B, Harding G et al (1987) X-ray diffraction measurements of some plastic materials and body tissues. Med Phys 14(4): 526–532.
46. Lewis RA, Hall CJ, Hufton AP et al (2003) X-ray refraction effects: application to the imaging of biological tissues. British J Radiol 76: 301–308.
47. Momose A, Fukuda J (1995) Phase-contrast radiographs of nonstained rat cerebellar specimen. Med Phys 22: 375–379.
48. Cloetens P, Ludwig W, van Dyck D, et al (1999) Quantitative phase tomography by holographic reconstruction. Proc SPIE 3772: 279–290.
49. Beckman F, Bonse U, Busck F et al (1997) X-ray microtomography (μCT) using phase contrast for the investigation of organic matter. J Comput Assist Tomogr 21: 539–553.
50. Chapman D, Thomlinson W, Johnston RE et al (1997) Diffraction enhanced x-ray imaging. Phys Med Biol 42: 20115–20125.

51. Momose A, Yashiro W, Takeda Y et al (2008) Sensitivity of x-ray phase tomography based on Talbot and Talbot-Lau interferometer. Proc SPIE 7078: 707811-1-707811-8.
52. Nugent KA, Gureyev TE, Cookson DJ et al (1996) Quantitative phase imaging using hard x-rays. Phys Rev Letters 77: 2961–2964.
53. Pfeiffer F, Weitkamp T, Bunk O et al (2006) Phase retrieval and differential phase-contrast imaging with low brilliance x-ray sources. Nature Physics 2: 256–261.
54. Wilkins SW, Gureyev TE, Gao D et al (1996) Phase-contrast imaging using polychromatic hard x-rays. Nature 384: 335–338.
55. Donnelly EF, Price RR, Lewis KG et al (2007) Polychromatic phase-contrast computed tomography. Med Phys 34: 3165.
56. Olivo A, Speller R (2007) Polychromatic phase contrast imaging as a basic step towards a widespread application of the technique. Nucl Instrum Methods A580: 0179–1082.
57. Olivo A, Speller R (2007) A coded-aperture technique allowing x-ray phase contrast imaging with laboratory sources. Appl Phys Lett 91: 074106.
58. Zhou SA, Brahme A (2008) Development of phase-contrast x-ray imaging techniques and potential medical applications. Physica Medica 24: 129–148.
59. Takeda T, Wu J, Yoneyama A et al (2004) SR biomedical imaging with phase-contrast and fluorescent x-ray CT. Proc SPIE 5535: 380–391.
60. Dilmanian FA, Garrett RF, Thomlinson WC et al (1990) Multiple energy computed tomography for neuroradiology with monochromatic-rays from the National Synchrotron Light Source. Physica Medica VI, n.3-4: 301–307.
61. Bond VP, Robertson JS, (1957) Vertebrate radiobiology (lethal actions and associated effects). Annu Rev Nucl Sci 7: 135–62.
62. Boone JM, Velazquez O, Cherry SR (2004) Small-animal x-ray dose from micro-CT. Mol Imaging 3: 149–158.
63. Carlson SK, Classic KL, Bender CE et al (2007) Small animal absorbed radiation dose from micro-computed tomography imaging. Mol Imaging Biol 9: 78–82.